IEEE Access
Multidisciplinary | Rapid Review | Open Access Journal

Received May 6, 2021, accepted June 16, 2021, date of publication June 21, 2021, date of current version June 29, 2021.

Digital Object Identifier 10.1109/ACCESS.2021.3090963

Medium-Wave Infrared Static Fourier Transform Spectrometer Based on Micro-Optical Elements

YUPENG CHEN[1,2], JINGUANG LV[1], BAIXUAN ZHAO[1,2], JIN TAO[1], YUXIN QIN[1], WEIBIAO WANG[1], AND JINGQIU LIANG[1]

[1]State Key Laboratory of Applied Optics, Changchun Institute of Optics, Fine Mechanics and Physics, Chinese Academy of Sciences, Changchun 130033, China
[2]Daheng College, University of Chinese Academy of Sciences, Beijing 100049, China

Corresponding authors: Jingqiu Liang (liangjq@ciomp.ac.cn) and Jinguang Lv (jinguanglv@163.com)

This work was supported in part by the National Natural Science Foundation of China under Grant 61805239, Grant 61627819, Grant 61575193, and Grant 61727818; in part by the Jilin Scientific and Technological Development Program under Grant 20190303063SF, Grant 20180201024GX, and Grant 20150520101JH; and in part by the Youth Innovation Promotion Association Foundation of the Chinese Academy of Sciences under Grant 2018254.

ABSTRACT In recent years, various fields have established an urgent need for real-time online measurement of infrared spectra. To this end, reducing the weight and size of infrared spectrometers is particularly important. This paper reports a micro-optical element static Fourier transform spectrometer (MOESFTS) with a working wavelength from 3.7 μm to 4.8 μm. This spectrometer is entirely composed of micro-optical elements, and its interference system comprises stepped micromirrors and a lightweight beam splitter to realize a lightweight, miniaturized instrument capable of static real-time spectrum measurements. The micro-optical element microlens array leads to the acquisition of interferogram in the form of two-dimensional point-array in the MOESFTS. Therefore we establish a field-of-view integral model of the interference-image point intensity to analyze the influence of the field of view on the reconstructed spectrum. We complete the optical design of the micro-optical collimator (MOC) lens and the micro-optical relay (MOR) lens. And an effective processing algorithm for spectral reconstruction from two-dimensional point-array is presented. A prototype was designed and constructed, and spectral calibration was completed. The spectra of acetonitrile (CH_3CN) and carbon dioxide (CO_2) were measured, the experimental results show that the spectral peak drift errors were found to be less than 0.18%.

INDEX TERMS Fourier transform spectrometer, lightweight, medium-wave infrared, miniaturization, micro-optical element, spectral measurement.

I. INTRODUCTION

Fourier transform spectrometers (FTSs) have the advantages of being multichannel (the Fellgett advantage) and having a high throughput (the Jacquinot advantage). They are widely used in the biopharmaceutical, food safety, and environmental-monitoring fields [1]–[8]. The continuous advancement of science and technology has gradually improved the performance of FTSs; However, various fields have put forward an urgent requirement for real-time online measurement of spectra in emergency situations and severe environments. Spatially modulation FTSs contain no moving parts, making their structure more stable and giving them a stronger ability to achieve transient-target spectral detection. Therefore, while traditional temporally modulation FTSs continue to be developed, attention has also been paid to the original method of static spatially modulation FTS measurements. Developments have focused on decreasing the size and weight of the instruments to further adapt them to the application requirements of real-time online monitoring [9]–[12].

In the 1990s, Linkemann *et al.* found that multiple equally spaced optical path difference (OPD) sampling points will be distributed in space when two coherent beams are reflected and superimposed by two symmetrically inclined reflection planes. Based on this, an FTS without moving parts was proposed [13]. Subsequently, Moeller proposed a design concept replacing the inclined reflection planes with stepped mirrors, which solved the energy losses that result from the use of inclined reflection planes. This stepped mirror structure provided a new method to realize spatially modulation FTSs [14], [15].

The associate editor coordinating the review of this manuscript and approving it for publication was Mira Naftaly.

Based on the design concept proposed by Moeller, in 2011, Feng *et al.* proposed the structure of a static Fourier transform spectrometer (SFTS) instrument based on a stepped mirror. They studied the diffraction effects of stepped mirrors and theoretically demonstrated the feasibility of their miniaturization [16], [17]. In 2012 Zheng *et al.* researched manufacturing technology for producing miniaturized lower-stepped micromirrors and applied microelectromechanical systems(MEMS) technology to their production, reducing their volume and weight [18]. Chen and Zhang conducted theoretical and manufacturing research on the higher-stepped micromirror and beam splitter, and they built an SFTS system on an optical platform to obtain a two-dimensional interferogram [19], [20].

In response to the urgent need for miniaturization of SFTS devices for online monitoring and transient-target spectrum measurements, in this paper, we propose a medium-wave infrared SFTS based on micro-optical elements. This is a lightweight and miniaturized spectrometer with high performance and excellent environmental adaptability. We discuss the influence of the field of view on the reconstructed spectrum of this micro-optical element SFTS (MOESFTS) and present the design and optimization of its micro-optical element system. In this work, interferogram-processing and spectrum-reconstruction methods for the MOESFTS were established, and we completed the construction of a prototype instrument. We also performed spectrum-measurement experiments, and the results demonstrate that the measured spectra of CH_3NH and CO_2 almost completely coincide with the reference spectra from a commercial FTS system.

II. STRUCTURE AND PRINCIPLE OF MOESFTS

Fig. 1 shows an optical schematic diagram of the MOESFTS instrument. This comprises a medium-wave infrared light source covering a wavelength band from 3.7 μm to 4.8 μm, a micro-optical collimator (MOC) lens, a miniature interference system, a micro-optical relay (MOR) lens, and a medium-wave infrared array detector. The miniature interference system comprises stepped micromirrors and a lightweight beam splitter. The MOR comprises a microlens array (MLA) and a relay lens (RL).

The working principle of the system as follows. Light from the infrared source is incident on the miniature interference system after being collimated by the MOC. It is then split by the lightweight beam splitter into two beams with equal intensity, and these are transmitted to the lower-stepped and higher-stepped micromirrors to achieve phase modulation. The two reflected beams with spatially phase-modulation information then return to the beam splitter to interfere. The interference beams propagate and are coupled by the MOR to the array detector to form an interferogram in the form of a two-dimensional point array.

In the miniature interference system, the higher-stepped and lower-stepped micromirrors are located symmetrically with respect to the lightweight beam splitter, and the steps are arranged orthogonal to one another. Therefore,

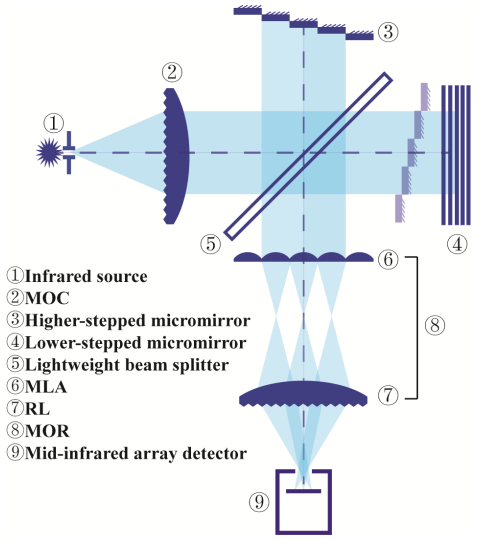

FIGURE 1. Optical schematic diagram of the MOESFTS instrument.

$N \times N$ phase-modulation units are formed by these micromirrors, where N is the maximum number of substeps of the micromirrors.

The phase-modulation unit (m, n) formed by the mth substep of the higher-stepped micromirror and the nth substep of the lower-stepped micromirror, which is placed orthogonally, leads to an optical path difference (OPD) that can be expressed as $\delta(m, n)$ between the two beams reflected by the mth and nth substeps such that $\delta(m, n) = 2(Nm - n)d$, where d is the height of lower substeps and Nd is the height of the higher substeps. The two beams interfere with each other, and the resulting interference intensity is expressed as $I_{\delta(m,n)}$. The design heights of the two kinds of substeps satisfy the Nyquist–Shannon sampling theorem, and a two-dimensional $N \times N$ point-array interferogram will be obtained by the detector while measuring a spectrum using the MOESFTS. Image preprocessing is performed on the point-array interferogram to obtain the interference-image point-intensity sequence I_δ. The Fourier transform of I_δ is taken to reconstruct the spectrum as

$$B(\sigma) = \mathscr{F}\{I_\delta - I_0\} = \int_{-\infty}^{+\infty} (I_\delta - I_0)\, e^{-i2\pi\sigma\delta} d\delta \qquad (1)$$

where $B(\sigma)$ is the reconstructed spectrum and I_0 is the DC offset of the measured interferogram.

III. MOESFTS SYSTEM DESIGN

A. STEPPED MICROMIRROR DESIGN

The wavelength band of MOESFTS is from 3.7 to 4.8 μm, and the theoretical spectral resolution can be expressed as $\Delta\sigma_0 = 7.8\ \text{cm}^{-1}$. According to the Nyquist–Shannon principle, the OPD sampling interval for the interference-image point-intensity sequence must meet the criterion $2d < 1.5\ \mu$m. If the maximum OPD is $\delta_{\max}$, this will give a relationship with spectral resolution of $\Delta\sigma_0 = 1/\delta_{\max}$, and

the maximum OPD generated by the Nth higher substep and the Nth lower substep can be expressed as $\delta_{\max} = 2N^2 d$. According to this relation, considering the manufacture of the stepped micromirrors and the requirements of spectral resolution, the design parameters of the stepped micromirrors can be calculated, and these are shown in Table 1.

TABLE 1. Design parameters of the stepped micromirrors.

Design Parameter	Value
Largest step order	32
Higher substep height/μm	20
Lower substep height/μm	0.625
Substep width/mm	1
$\delta_{\max}/\mu$m	1280

B. FIELD-OF-VIEW ANALYSIS AND MOC DESIGN

To increase the luminous flux of the MOESFTS system, it is necessary to increase its field of view. However, increasing the field of view will broaden the spectrum and reduce the spectral resolution [21]. Because MOESFTS introduces a micro-optical element MLA and uses its spatially modulation characteristics, there is a one-to-one correspondence between the closely spaced phase-modulation units and the closely spaced microlens units of the MLA. As such, increasing the field-of-view angle will lead to crosstalk between the interference intensity information of adjacent units, reducing the spectral resolution and also distorting the spectrum. Therefore, it is necessary to consider not only spectral broadening but also spectral distortion caused by this crosstalk.

Fig. 2(a) shows a schematic diagram of the transmission process of a single spectral-channel beam. If the light emanates from an ideal point source, the MOC only emits the collimated beam in the center field of view along the optical axis, that is, the blue beam in Fig. 2(a). We designed the shape and size of each microlens unit of the MLA to be the same as that of its corresponding phase-modulation unit to ensure that each interference-image point will only contain the interference-intensity information from a single phase-modulation unit.

In reality, however, the light source will be an extended rather than a point source. In addition to the collimated beam from the center field of view along the spectral axis of the MOC, there are therefore also collimated beams emitted from every off-axis field of view. That is, the red beam in Fig. 2(a), which is emitted from the sagittal edge field of view, and the yellow beam, which is emitted from the tangential edge field of view. The collimated beams emitted from the sagittal and tangential edge fields of view are both reflected back to the lightweight beam splitter by two adjacent substep surfaces when they are transmitted to the stepped micromirror. The intensity of the interference-image point formed by the beams of the two fields of view is obtained

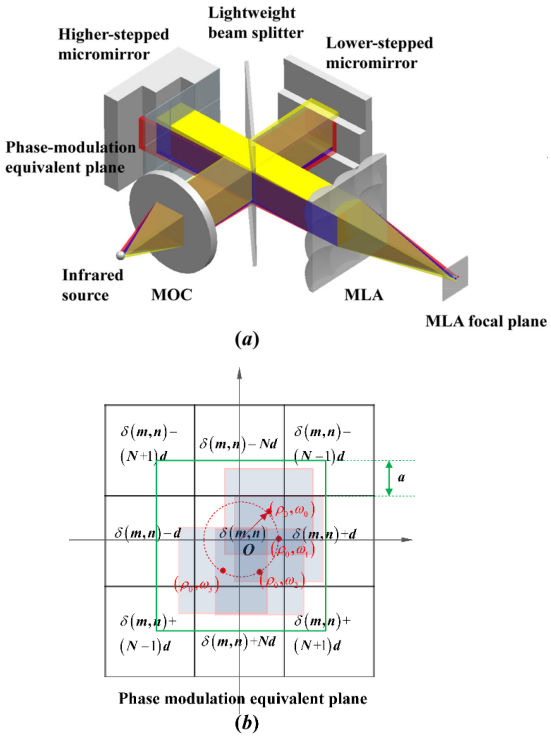

FIGURE 2. (a) Schematic diagram of single spectral channel beam-transmission process. (b) Subfield of view distribution on the phase-modulation equivalent plane.

on the focal plane of the MLA. Each image point will contain the interference-intensity information from two adjacent phase-modulation units. The larger the angle of view, the more serious this crosstalk of interference-intensity information and the larger the spectral broadening.

To determine the design parameter index of the field of view ω of the MOESFTS system, it is necessary to first determine the relationship between the spectral-broadening range, the degree of spectral distortion, and the field of view. The spectral-broadening range is the wave number for spectral broadening, expressed as $\Delta\sigma$, and we introduce the normalized spectral error constant NSEC to evaluate the degree of spectral distortion, which is expressed as:

$$\mathrm{NSEC} = \sum_{\sigma_{min}}^{\sigma_{max}} \frac{|B(\sigma) - B_0(\sigma)|}{|B_0(\sigma)|}, \tag{2}$$

where $B_0(\sigma)$ is the reference spectrum. The larger the NSEC of a spectrum, the more severe the spectral distortion.

This paper proposes a field-of-view integral model of the interference-image point intensity to obtain the value of $\Delta\sigma$ and the NSEC of spectra obtained with different ω values. The model for this is as shown in Fig. 2(b). We locate all the phase-modulation units on a single plane, termed the phase-modulation equivalent plane. Establishing a polar coordinate system on this plane, the origin of coordinate system O is the central point of phase-modulation unit (m, n). In response to the unique structure of the MLA, the field of

view of each microlens unit [the green rectangular field of view in Fig. 2(b)] is divided into multiple subfields of view [the red rectangular field of view in Fig. 2(b)], which are expressed as (ρ_x, ω_y). The intensity of the interference-image point formed on the focal plane of a microlens unit is obtained by integration of the intensity of the image point of the collimated beam of each subfield of view, as:

$$I_{\delta(m,n)} = \int_0^a \int_0^{2\pi} I\left(\rho_x, \omega_y\right) d\rho_x d\omega_y, \tag{3}$$

where a is the displacement between the central point of the off-axis edge subfield of view and the central point of the on-axis central subfield of view. The relationship between a and l, which is the distance from the MLA to the phase-modulation equivalent plane such that $a = l\tan(\omega)$. The function $I(\rho_x, \omega_y)$ represents the intensity of the image point of the outgoing collimated beam of the subfield of view (ρ_x, ω_y), and $I_{\delta(m,n)}$ is the intensity of the image point of phase-modulation unit (m, n).

Although in this case we do not know $I(\rho_x, \omega_y)$, we can derive it. Taking the subfield of view (ρ_0, ω_0) in Fig. 2(b) as an example, (ρ_0, ω_0) represents the red rectangular subfield of view whose center point polar coordinate is (ρ_0, ω_0). The collimated beam of (ρ_0, ω_0) is modulated by four phase-modulation units, specifically (m, n), $(m, n-1)$, $(m+1, n-1)$, and $(m, n+1)$. The intensity of the image point of the collimated beam of (ρ_0, ω_0) is then:

$$\begin{aligned} &I\left(\rho_0, \omega_0\right) \\ &= B\left(\sigma\right)\cos\left(2\pi\sigma\delta\left(m+1, n-1\right)\right)\rho_0^2\cos\omega_0\sin\omega_0 \\ &\quad + B\left(\sigma\right)\cos\left(2\pi\sigma\delta\left(m, n-1\right)\right)\rho_0^2\left(1-\cos\omega_0\right)\sin\omega_0 \\ &\quad + B\left(\sigma\right)\cos\left(2\pi\sigma\delta\left(m+1, n\right)\right)\rho_0^2\cos\omega_0\left(1-\sin\omega_0\right) \\ &\quad + B\left(\sigma\right)\cos\left(2\pi\sigma\delta\left(m, n\right)\right)\rho_0^2\left(1-\cos\omega_0\right)\left(1-\sin\omega_0\right), \end{aligned} \tag{4}$$

According to (3) and (4), we can obtain the intensity distribution of the interference-image point array. Performing image preprocessing on this and taking the Fourier transform to obtain the spectrum $B(\sigma)$, we can then also obtain the values of $\Delta\sigma$ and NSEC. By changing ω, the values of $\Delta\sigma$ and NSEC at different ω values are calculated from the field-of-view integral model of the interference-image point intensity. In this way, the fitted curves shown in Fig. 3(a) were obtained.

While satisfying the conditions $\Delta\sigma \leq 8\ \mathrm{cm}^{-1}$ and NSEC ≤ 0.1, we try to increase the angle of field of view to ensure sufficient luminous flux for the spectrometer. The field of view of the MOESFTS system was determined to be $\omega = 0.5°$, and this also determines the field of view of the MOC, expressed as ω_{MOC}. The main parameters of the MOC are shown in Table 2.

A diffractive–refractive lens was adopted for the optimized MOC design. Simulation results showed that the extended angle of the collimated beam from each field of view of the MOC is less than 0.037 mrad. We tested the produced diffractive–refractive lens MOC by using it to collimate

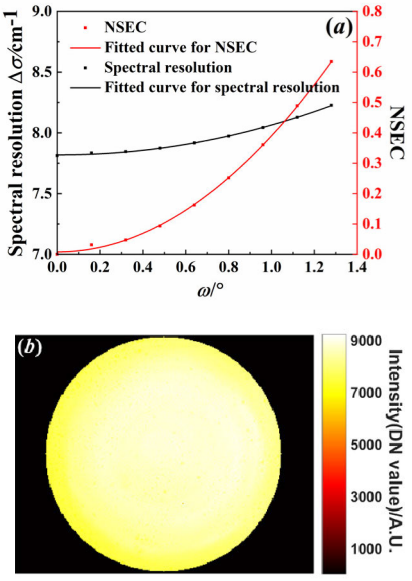

FIGURE 3. (a) Fitted curves showing the relationship between the $\Delta\sigma$ and NSEC values of the reconstructed spectrum and the field of view of the MOC, ω. (b) Intensity distribution of the collimated beam emitted from the MOC on the area array detector.

TABLE 2. Main design parameters of the MOC.

Parameter	Value
Wavelength/μm	3–5
Diameter/mm	45
Focal length/mm	110
Field angle ω_{MOC}/deg	0.5

beams emitted from the infrared light source. The intensity distribution of the collimated beam on the array detector is shown in Fig. 3(b), and the standard deviation of the test intensity was 202.73 digital number (DN) value. The uniformity of the illumination was 97.7%, which indicates that the beams emitted from the MOC lens have good collimation performance and illumination uniformity.

C. MOR DESIGN

The design of the MOR system can be divided into two sections: the design of the MLA and the design of the RL. As described in Section III-A, the MLA modulates the interference beam emitted from the miniature interference system into an interference-image point array and then couples this to the array detector through the RL for secondary imaging. The number, shape, and size of the microlens units in the MLA are the same as those of the corresponding phase-modulation units. The RL is an object-space telecentric system, and this adopts micro-optical elements which is a binary diffraction lens to realize. The MOR and infrared array detector must meet the cold stop matching requirement to suppress the

TABLE 3. Main parameters of the infrared array detector.

Parameter	Value
Wavelength/μm	3.7–4.8
Pixels	320 × 256
Pixel size/μm	30
Cold stop diameter/mm	5.1
$F^{\#}$	4

TABLE 4. Main parameters of the MLA.

Parameter	Value
Shape	Cube
Unit Number	32 × 32
Unit diameter/mm	1
Image space NA/NA$_i$	0.03
Focal length/mm	23.6

TABLE 5. Main parameters of the RL.

Parameter	Value
Object height/mm	22.6
β	0.24
RMS radius/μm	≤120
Object space NA/NA$_i$	0.03
Field angle ω_{MOR} /deg	0.5
Temperature/°C	−20 to 60

negative effects of stray light. Table 3 shows the main parameters of the infrared array detector.

To match the MLA and the RL, it necessary that the image-space numerical aperture of the MLA, expressed as NA$_i$, is equal to the object numerical aperture of the RL, expressed as NA$_o$. The value of NA$_o$ can be calculated from the magnification of the MOR (β) and the value of $F^{\#}$ shown in Table 3. According to Tables 1 and 2, we can obtain $\beta = 256 \times 30/1000 \times 32 = 0.24$. Then, $\mathrm{NA_o} = \beta/2F^{\#} = 0.03$ and $\mathrm{NA_o} = \mathrm{NA}_i = 0.03$. Therefore, the focal length of the MLA, f_1, can be obtained from the aperture diameter of the MLA microlens unit. The main parameters of the MLA are as shown in Table 4. We can see that the field of view of the MOR is equal to that of the MOC due to the combination of the MOR with the miniaturized interference system.

The RL is a micro-optical element, the back surface of which is the binary diffraction surface. It is made from a kind of chalcogenide glass that can realize an athermal design and simpler processing of the binary diffraction surface. Table 5 lists the main parameters of the RL. The root-mean-square (RMS) radius of the image points must be less

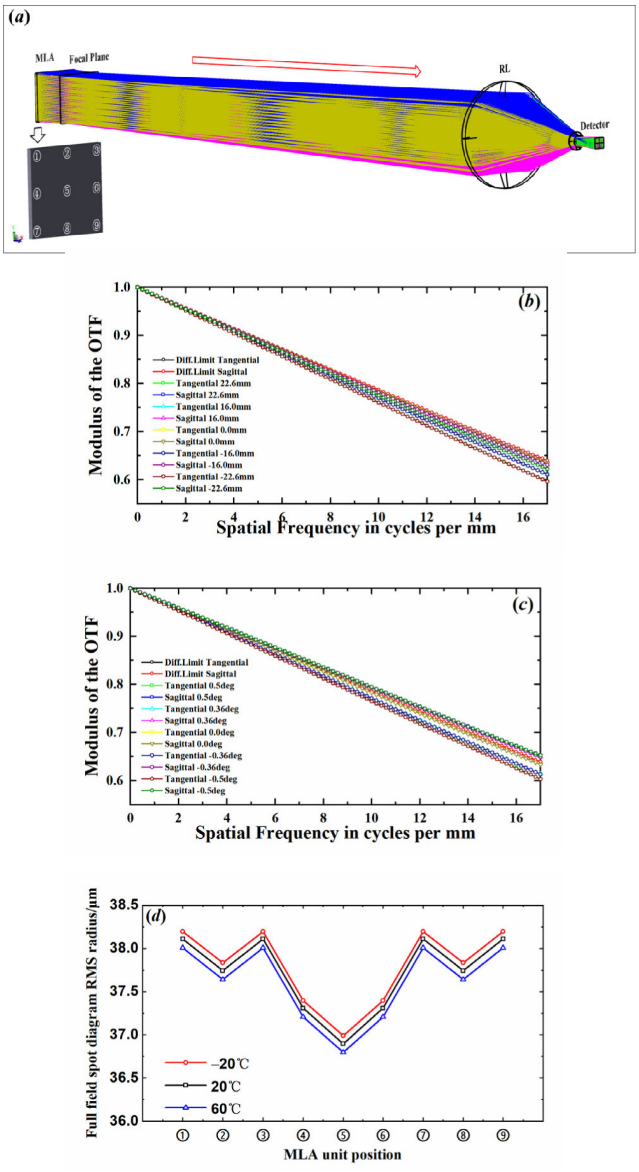

FIGURE 4. (a) Ray-tracing diagram of the MOR and representative microlens units selected on the MLA. (b) MTF curve of the RL. (c) MTF curve of the MOR. (d) Full-field RMS radius of the interference-image point corresponding to each microlens unit selected at temperatures of −20°C, 20°C, and 60°C.

than the width of four detector pixels to ensure that the interference-image points from adjacent spectral channels are not aliased. The exit pupil position of the MOR must coincide with the cold stop position of the detector.

We optimized the design of the MOR according to the parameters and requirements above. A ray-tracing diagram of the MOR was obtained by simulation, and this is shown in Fig. 4(a). Several representative micro-lens units of the MLA were selected to evaluate the design of the MOR, and the full-field RMS radius of the interference-image point formed by the incident beam was used as the basis of this evaluation.

As illustrated in Fig. 4(a), nine microlens units were selected, among which ①, ③, ⑦, and ⑨ are diagonal units,

② and ⑧ are tangential edge units, and ④ and ⑥ are sagittal edge units. Fig. 4(b) and 4(c) show the modulation transfer functions (MTFs) of the RL and the MOR, which are both greater than 0.6. Fig. 4(d) shows the full-field RMS radius of the interference-image point corresponding to each microlens unit selected at temperatures of −20°C, 20°C, and 60°C, which are all less than 120 μm. This indicates that the MOR has achieved an achromatic and athermalized design, and the result meets the various requirements of the parameters.

IV. SPECTRUM-RECONSTRUCTION PROCESSING

Based on the results of the designs of the stepped micromirrors, the MOC, and the MOR, we simulated the structure and light-field propagation of the MOESFTS system. An image point-array interferogram of a monochromatic light source was obtained, and this is shown in Fig. 5.

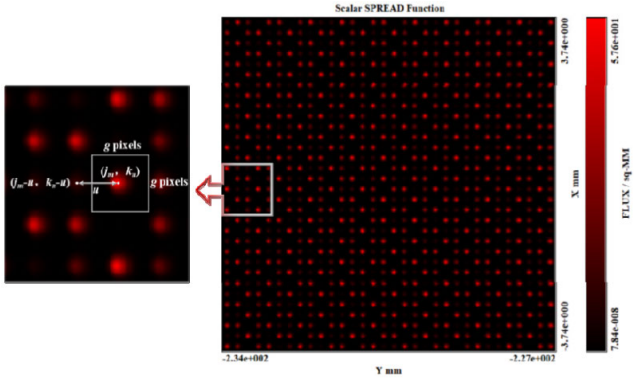

FIGURE 5. Image point-array interferogram obtained by simulation.

The two-dimensional interferogram should be reprocessed to obtain a one-dimensional interferogram for reconstruction of the spectrum, and this is called dimension reduction [22]. Choosing an interference-image point corresponding to a certain phase-modulation unit (m, n), we set the central pixel coordinate as (j_m, k_n). We take the mean value of the $g \times g$ neighbor pixel intensities of the (j_m, k_n) as the interference-image point intensity $I_{\delta(m,n)}$, where g is the number of pixels occupied by the phase-modulation unit at which an interference-image point is located.

We suppose the coordinate difference between the center pixels of any adjacent interference-image point is u; that is, the central pixel of the interference-image point corresponding to the phase-modulation unit $(m + p, n + q)$ is expressed as $(j_m + up, k_n + uq)$. In this way, we complete the central-pixel addressing of each interference-image point, and the intensity of all interference-image points can be obtained. The dimension-reduction reprocessing can then obtain the one-dimensional interference-image point-intensity sequence from the two-dimensional image point-array interferogram.

It is also necessary to remove the DC offset of the one-dimensional interference-image point-intensity sequence. The ideal intensity of the DC offset of each interference-image point will be equal; However, in actual

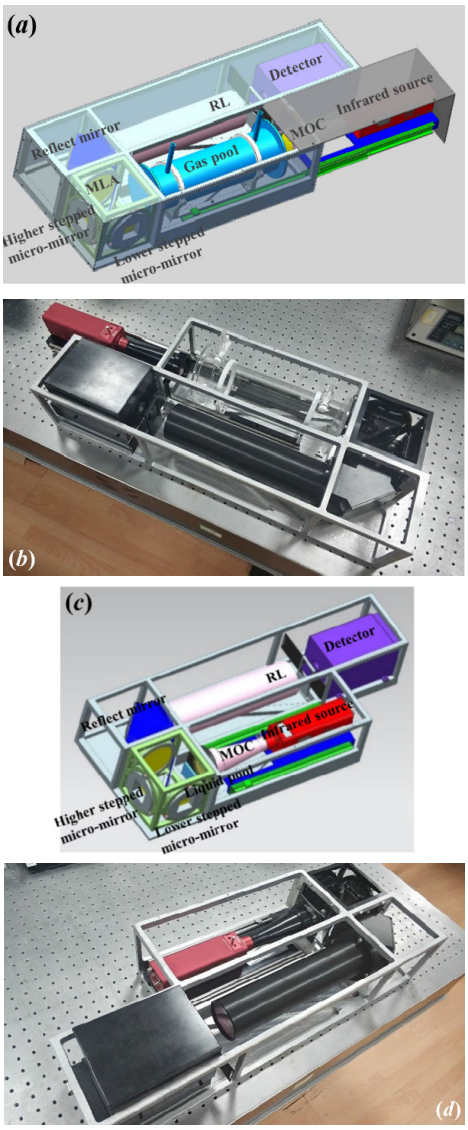

FIGURE 6. (a) Structure diagram of the MOESFTS system for gas measurements. (b) Photograph of the prototype MOESFTS system used for gas measurements. (c) Structure diagram of the MOESFTS system used for liquid measurements. (d) Photograph of the prototype of the MOESFTS system used for liquid measurements.

conditions, factors such as instability of the light source or system errors will cause changes in the intensity of the DC offset of each interference-image point. By fitting the interference-image point-intensity sequence, the DC offset of each interference-image point can be obtained and it can be removed from the intensity sequence to correct the spectral error.

We take the coordinates of the maximum interference-image point intensity $I_{\delta(m,n)\max}$ as the origin, and the OPD δ of each phase-modulation unit has a one-to-one correspondence with interference-image point intensity $I_{\delta(m,n)}$. Selecting the appropriate window function to apodize the interference-image point-intensity sequence, we can suppress spectral side-lobe oscillation. The interference-image point-intensity sequence I_δ that matches the OPD sequence

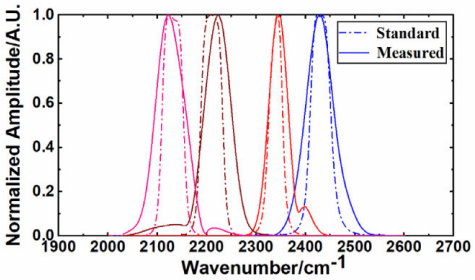

FIGURE 7. Measured narrowband light-source spectra after calibration.

is then obtained, and substituting I_δ into (1), we can get the reconstructed spectrum.

V. EXPERIMENTAL RESULTS

A. MOESFTS PROTOTYPE

We completed the manufacture of the micro-optical elements such as the MOC, the miniaturized interference system, and the MOR. The overall layout of the MOESFTS prototype was designed, and the assembly and adjustment of the prototype was completed. To further reduce the volume of the prototype, we used an infrared mirror to fold the optical path of the MOR system. In addition, a slide rail was introduced into the mechanical structure of the sample cell to make the MOESFTS system compatible with gas and liquid sample cells. Fig. 6(a) and 6(b) show a structure diagram and a photograph of the prototype system used for gas measurements, respectively, and Fig. 6(c) and 6(d) show a structure diagram and a photograph of the system used for liquid measurements.

B. SPECTRAL CALIBRATION

We used a black-body light source to perform spectral calibration on the MOESFTS, inserting different narrowband filters in the optical path to form a narrowband light source. The parameters of the four filters used were central wave number 2124 cm^{-1} with bandwidth 45.1 cm^{-1}, central wave number 2208 cm^{-1} with bandwidth 46 cm^{-1}, central wave number 2343 cm^{-1} with bandwidth 29.9 cm^{-1}, and central wave number 2424 cm^{-1} with bandwidth 44.4 cm^{-1}. We performed spectrum measurements using these four narrowband light sources and carried out least-squares fitting between the measured and theoretical peak positions to obtain the offset and gain coefficients. We then calibrated the measured peak positions with these coefficients and measured the narrowband light-source spectra again. The results of this calibration are shown as the solid lines in Fig. 7, in which the dashed lines indicate the theoretical spectrum curves.

The numerical results of the spectral peak position calibration are shown in Table 6. The maximum peak position error was 14 cm^{-1}, and the maximum peak position shift was 0.63%.

C. SAMPLE SPECTRUM MEASUREMENT

We performed spectrum measurements of anhydrous CH_3NH with a mass fraction greater than 99.7%, and the resulting

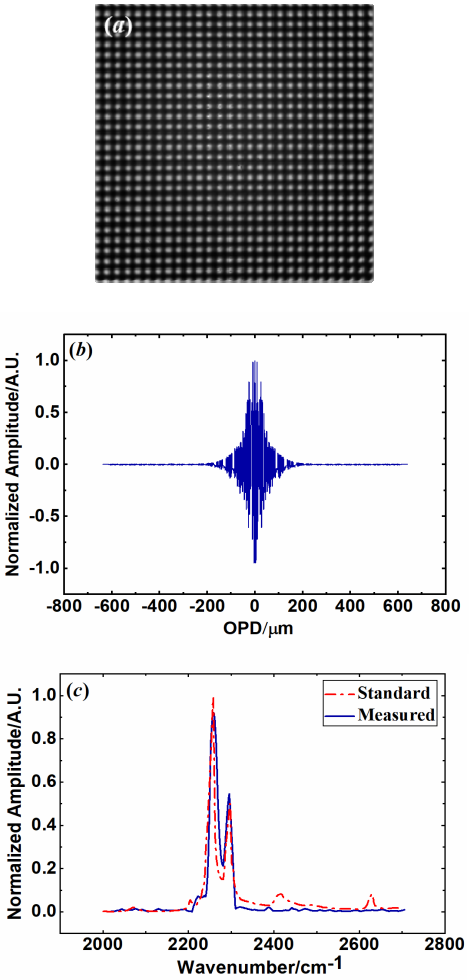

FIGURE 8. (a) Point image array interferogram of the measured CH_3NH (b) Normalized interference-image point-intensity sequence. (c) Spectrum curve of CH_3NH measured by MOESFTS.

TABLE 6. Results of the spectral peak position calibration.

Standard Wave Number/ cm^{-1}	Measured Wave Number/ cm^{-1}	Wave Number Error/ cm^{-1}	Peak Shift/ %
2124	2122	2	0.09
2208	2222	14	0.63
2343	2342	1	0.04
2424	2430	6	0.25

interferogram is shown in Fig. 8(a). This was then preprocessed to obtain the interference-image point-intensity sequence by removing the DC offset and addressing and apodizing with a Blackman function. The resulting normalized interference-image point-intensity sequence is shown in Fig. 8(b). We then took the Fourier transform of this intensity sequence to obtain a spectrum curve for the anhydrous CH_3NH, and this is shown in Fig. 8(c).

We also performed a spectrum measurement of CO_2 gas with a concentration of 99%, and the resulting interferogram is shown in Fig. 9(a). Again, the normalized

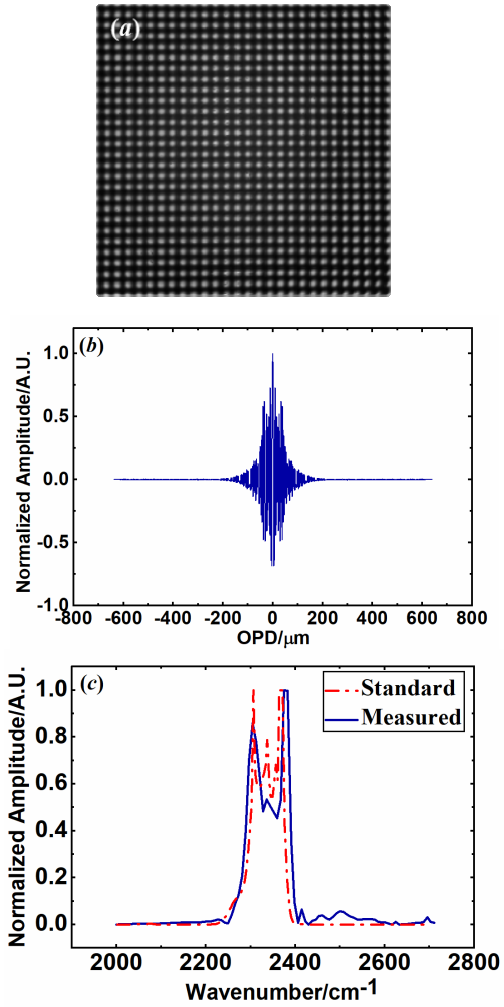

FIGURE 9. (a) Point image array interferogram of the measured CO_2. (b) Normalized interference-image point-intensity sequence. (c) Spectrum curve of CO_2 measured by MOESFTS.

interference-image point-intensity sequence is shown in Fig. 9(b), and the final spectrum curve obtained by Fourier transform is shown in Fig. 9(c). In Fig. 8(c) and 9(c), the solid lines indicate the sample spectra measured by the MOESFTS prototype, while the dashed lines show the standard reference spectra of each sample. The standard spectrum data were all derived from the measurement results obtained using a Bruker VERTEX 70v temporally modulation FTS with the measured spectral resolution set to 8 cm^{-1}. The sampling time was 1 min.

The numerical results of the MOESFTS sample measurement data are shown in Table 7. The spectral peak positions of the CH_3NH were 2261 cm^{-1} and 2296 cm^{-1}, and the drift errors compared with the standard spectral peak positions were 0.18% and 0.09%. The spectral peak positions of the CO_2 were 2302 cm^{-1} and 2333 cm^{-1}, for which the drift errors were both 0.17%.

Generally speaking, if the shift in the spectral peak position is less than half of the spectral resolution, it is considered that the spectral accuracy requirement is met. The spectral

TABLE 7. Results of the spectra measured By MOESFTS.

Sample	Standard Wave Number/ cm^{-1}	Measured Wave Number/ cm^{-1}	Wave Number Error/ cm^{-1}	Peak Shift/ %
CH_3NH	2257	2261	4	0.18
	2298	2296	2	0.09
CO_2	2306	2302	4	0.17
	2337	2333	4	0.17

resolution of MOESFTS is 8 cm^{-1}, so the spectral peak position error is required to be less than 4 cm^{-1}. The experimental results show that the spectral peak position errors of all the measured spectra are less than 4 cm^{-1}. This indicates that the MOESFTS system meets the spectral accuracy requirements.

VI. CONCLUSION

This paper reports the design and construction of a lightweight, miniature medium-wave infrared SFTS based on micro-optical elements. The miniaturized interference system is composed of stepped micromirrors and a lightweight beam splitter, which realizes static phase modulation to ensure high stability. We proposed a field-of-view integral model of the interference-image point intensity, and the influence of the field of view on the spectrum was analyzed. The system design parameters were obtained, and a prototype was designed and constructed. A spectrum-reconstruction algorithm suitable for the image point-array interferogram was established.

Spectral calibration of the MOESFTS prototype was conducted, and spectrum measurements of CH_3NH and CO_2 were performed. The measured spectra were found to coincide with the standard reference spectra measured by a commercial temporally modulation FTS system. The peak shifts for CH_3NH were 0.18% and 0.09%, and the peak shifts for CO_2 were both 0.17, meeting the spectral accuracy requirements.

In future work, we will perform intensity calibration of the MOESFTS system to realize quantitative detection of substances. Regarding the algorithms, further research into spectral denoising and enhancement of the spectral resolution will be carried out to achieve high-sensitivity detection of substances.

REFERENCES

[1] O. F. Sarioglu, Y. T. Tamer, A. D. Ozkan, H. I. Atabay, C. Molva, and T. Tekinay, "Fourier transform infrared spectroscopy as a novel approach for analyzing the biochemical effects of anionic surfactants on a surfactant-degrading arcobacter butzleri strain," *Appl. Spectrosc.*, vol. 67, no. 3, pp. 342–348, 2013.

[2] Y. Liu and H.-J. Kim, "Comparative investigation of secondary cell wall development in cotton fiber near isogenic lines using attenuated total reflection Fourier transform infrared spectroscopy (ATR FT-IR)," *Appl. Spectrosc.*, vol. 73, no. 3, pp. 329–336, Mar. 2019.

[3] H. Kobayashi, A. Shimota, C. Yoshigahara, I. Yoshida, Y. Uehara, and K. Kondo, "Satellite-borne high-resolution FTIR for lower atmosphere sounding and its evaluation," *IEEE Trans. Geosci. Remote Sens.*, vol. 37, no. 3, pp. 1496–1507, May 1999.

[4] R. A. Martinez, K. Guo, T. Zhai, F. L. Terry, L. E. Pierce, M. N. Islam, R. Gibson, J. M. Reed, R. G. Bedford, L. Maksymiuk, M. J. Freeman, B. A. Gorin, N. P. Christian, and A. I. Ifarraguerri, "Active mid-wave to long-wave supercontinuum FTIR sensor for standoff chemical detection," *J. Lightw. Technol.*, vol. 37, no. 14, pp. 3626–3636, Jul. 15, 2019.
[5] T. Liu, H. Liu, Y.-F. Li, Z. Chen, Z. Zhang, and S. Liu, "Flexible FTIR spectral imaging enhancement for industrial robot infrared vision sensing," *IEEE Trans. Ind. Informat.*, vol. 16, no. 1, pp. 544–554, Jan. 2020.
[6] P. Tao, P. Aihong, H. Wenjie, Y. Hao, and H. Yun, "FTIR/ATR spectroscopy applied to the rapid analysis for hemoglobin in human soluble blood samples," presented at the 3rd Int. Conf. Meas. Technol. Mechatronics Automat., 2011.
[7] G. Parodi, P. Dickerson, and J. Cloud, "Pollen identification by Fourier transform infrared photoacoustic spectroscopy," *Appl. Spectrosc.*, vol. 67, no. 3, pp. 342–348, Mar. 2013.
[8] B. Zhao, J. Lv, J. Ren, Y. Qin, J. Tao, and J. L. W. Wang, "Data procesing and performance evalution of a tempo-spatially mixed modulation imaging Fourier transform spectrometer based on stepped micro-mirror," *Opt. Exp.*, vol. 28, no. 5, pp. 6320–6336, 2020.
[9] A. Lacan, F.-M. Bréon, A. Rosak, F. Brachet, L. Roucayrol, P. Etcheto, C. Casteras, and Y. Salaün, "A static Fourier transform spectrometer for atmospheric sounding: Concept and experimental implementation," *Opt. Exp.*, vol. 18, no. 8, p. 8311, Apr. 2010.
[10] M. Erfan, Y. M. Sabry, and B. Mortada, "Mid infrared MEMS FTIR spectrometer," presented at the MOEMS Miniaturized Syst. 15th Int. Soc. Opt. Photon., vol. 9760, 2016, Art. no. 97600K.
[11] G. Boer, P. Ruffieux, T. Scharf, P. Seitz, and R. Dändliker, "Compact liquid-crystal-polymer Fourier-transform spectrometer," *Appl. Opt.*, vol. 43, no. 11, p. 2201, 2004.
[12] W. Wang, S. R. Samuelson, J. Chen, and H. Xie, "Miniaturizing Fourier transform spectrometer with an electrothermal micromirror," *IEEE Photon. Technol. Lett.*, vol. 27, no. 13, pp. 1418–1421, Jul. 1, 2015.
[13] J. Linkmann, F. Romero-Borja, and H. O. Tittel, " 8th intl conf on Fourier transform spectroscopy," *Proc. SPIE*, vol. 1575, Mar. 1991, p. 184.
[14] K. D. Moeller, "Miniaturized wavefront-dividing interferometers without moving parts for field and space application," *Proc. SPIE*, vol. 1992, pp. 130–139, Dec. 1993.
[15] K. D. Moeller, "Wave-front-dividing array interferometers without moving parts for real-time spectroscopy from the IR to the UV," *Appl. Opt.*, vol. 34, pp. 1493–1501, 1995.
[16] C. Feng, B. Wang, Z. Liang, and J. Liang, "Miniaturization of step mirrors in a static Fourier transform spectrometer: Theory and simulation," *J. Opt. Soc.*, vol. 28, no. 1, pp. 128–133, Jan. 2011.
[17] C. Feng, J. Liang, and Z. Liang, "Spectrum constructing with nonuniform samples using least-squares approximation by cosine polynomials," *Appl. Opt.*, vol. 50, no. 34, pp. 6377–6383, Dec. 2011.
[18] Y. Zheng, J. Liang, and Z. Liang, "Design and fabrication of step mirrors used in Space-modulated Fourier Transform Infrared Spectrometer," *Opt. Exp.*, vol. 21, no. 1, pp. 884–892, 2013.
[19] C. Chen, J. Liang, Z. Liang, J. Lü, Y. Qin, C. Tian, and W. Wang, "Fabrication and analysis of tall-stepped mirror for use in static Fourier transform infrared spectrometer," *Opt. Laser Technol.*, vol. 75, pp. 6–12, Dec. 2015.
[20] M. Zhang, J. Liang, Z. Liang, J. Lv, Y. Qin, and W. Wang, "Fabraction and flatness error analysis of a low-stepped mirror in a static Fourier transform infrared spectrometer," *J. Opt. Technol.*, vol. 85, no. 9, pp. 582–589, 2018.
[21] V. Saptari. *Fourier-Transform Spectroscopy Instrument Engineering-TT61*. [Online]. Available: http://WWW.spiedigitallibrary.org/ebooks/
[22] J. Gao, Z. Liang, J. Liang, W. Wang, J. Lü, and Y. Qin, "Spectrum reconstruction of a spatially modulated Fourier transform spectrometer based on stepped mirrors," *Appl. Spectrosc.*, vol. 71, no. 6, pp. 1348–1356, Jun. 2017.

YUPENG CHEN was born in Huludao, Liaoning, China, in 1996. He received the B.S. degree from the Dalian University of Technology, China, in 2017. He is currently pursuing the Ph.D. degree with the Changchun Institute of Optics, Fine Mechanics and Physics, Chinese Academy of Sciences, Changchun, China. His main research interests include infrared optics design and physical optical analysis.

JINGUANG LV received the B.S. degree from the School of Physics, Jilin University, in 2004, and the Ph.D. degree from the Changchun Institute of Optics, Fine Mechanics and Physics, Chinese Academy of Sciences, in 2013. He is an Associate Professor and a Master Supervisor with the State Key Laboratory of Applied Optics, Changchun Institute of Optics, Fine Mechanics and Physics, Chinese Academy of Sciences. His research interests include micro optical systems, optical information processing, and coherent spectral imaging.

BAIXUAN ZHAO was born in Changchun, Jilin, China, in 1993. He received the B.S. degree in physics from Jilin University, China, in 2016. He is currently pursuing the Ph.D. degree in optics Changchun Institute of Optics, Fine Mechanics and Physics, Chinese Academy of Sciences, Changchun, China. His current research interest includes spectral data processing.

JIN TAO received the B.S. and Ph.D. degrees in measurement technology and instrument from Tianjin University, in 2010 and 2016, respectively. He is a Research Associate with the State Key Laboratory of Applied Optics, Changchun Institute of Optics, Fine Mechanics and Physics, Chinese Academy of Sciences. He is currently committed to the development and application of micro LED chips and the research of uncooled infrared detection chips based on micro nano resonators.

YUXIN QIN was born in Mudanjiang, Heilongjiang, in 1985. He received the B.S. degree in optical information science and technology and the M.S. degree in optical engineering from Harbin Engineering University, in 2008 and 2011, respectively. Since 2011, he has been with the State Key Laboratory of Applied Optics, Changchun Institute of Optics, Fine Mechanics and Physics, Chinese Academy of Sciences. His main research interests include infrared spectroscopy instrument optical design and assembly adjustment.

WEIBIAO WANG was born in Yangzhou, Jiangsu. He received the Ph.D. degree from the Changchun Institute of Optics, Fine Mechanics and Physics, Chinese Academy of Sciences, in 1999. He is currently a Researcher with the Changchun Institute of Optics. He is a Doctor, a Researcher, and a Doctoral Supervisor. His research interests include photonic crystal and micro-nano photonics, LED array chip integration and application, field emission materials, and electron emission characteristics.

JINGQIU LIANG received the B.S. degree in professional semiconductor physics and devices from the Department of Electronic Science, Jilin University, in 1984, and the Ph.D. degree from the Changchun Institute of Optics, Fine Mechanics and Physics, Chinese Academy of Sciences, in 2003. She is currently a Professor with the Changchun Institute of Optics, Fine Mechanics and Physics, Chinese Academy of Sciences. Her research interests include micro optical electro mechanical system (MOEMS) and micro-structure optics, Fourier transform spectrometer, Fourier transform imaging spectrometer, micro LED arrays, and devices in visible light communication systems.